

PAPER • OPEN ACCESS

## Radioactive 3D printing for the production of molecular imaging phantoms

To cite this article: Jonathan I Gear *et al* 2020 *Phys. Med. Biol.* **65** 175019

View the [article online](#) for updates and enhancements.



MR Safe  
4D Phantom  
for MRgRT

QUASAR<sup>MRI<sup>4D</sup></sup>  
BY MODUS CA

LEARN MORE ▶



## PAPER

## OPEN ACCESS

RECEIVED  
7 May 2020REVISED  
22 June 2020ACCEPTED FOR PUBLICATION  
8 July 2020PUBLISHED  
4 September 2020

Original content from this work may be used under the terms of the [Creative Commons Attribution 3.0 licence](#).

Any further distribution of this work must maintain attribution to the author(s) and the title of the work, journal citation and DOI.



# Radioactive 3D printing for the production of molecular imaging phantoms

Jonathan I Gear<sup>1</sup>, Craig Cummings, Jim Sullivan, Natalie Cooper-Rayner, Patrick Downs, Iain Murray and Glenn D Flux<sup>✉</sup>

Joint Department of Physics, The Royal Marsden NHSFT and Institute of Cancer Research, Sutton, United Kingdom

<sup>1</sup>Author to whom any correspondence should be addressed.

E-mail: [jgear@icr.ac.uk](mailto:jgear@icr.ac.uk)

**Keywords:** 3D printing, quality control, phantoms, PET, SPECT

## Abstract

Quality control tests of molecular imaging systems are hampered by the complexity of phantom preparation. It is proposed that radioisotopes can be directly incorporated into photo-polymer resins. Use of the radio-polymer in a 3D printer allows phantoms with more complex and reliable activity distributions to be produced whilst simplifying source preparation.

Initial tests have been performed to determine the practicality of integrating Tc-99m into a photo-polymer and example phantoms produced to test suitability for quality control. Samples of build and support resins were extracted from the print cartridges of an Objet30Pro Polyjet 3D printer. The response of the resin to external factors including ionising radiation, light and dilution with Tc-99m pertechnetate were explored. After success of the initial tests the radio-polymer was used in the production of different phantoms. Radionuclide dose calibrator and gamma camera acquisitions of the phantoms were used to test accuracy of activity concentration, print consistency, uniformity and heterogeneous reproducibility. Tomographic phantoms were also produced including a uniform hot sphere, a complex configuration of spheres and interlacing torus's and a hot rod phantom.

The coefficient of variation between repeat prints of a 12 g disk phantom was 0.08%. Measured activity within the disks agreed to within  $98 \pm 2\%$  of the expected activity based on initial resin concentration. Gamma camera integral uniformity measured across a 3D printed flood field phantom was 5.2% compared to 6.0% measured with a commercial Co-57 flood source. Heterogeneous distributions of activity were successfully reproduced for both 2D and 3D imaging phantoms. Count concentration across regions of heterogeneity agreed with the planned activity assigned to those regions on the phantom design.

3D printing of radioactive phantoms has been successfully demonstrated and is a promising application for quality control of Positron Emission Tomography and Single Photon Emission Computed Tomography systems.

## 1. Introduction

Performance tests of molecular imaging systems are required at installation, acceptance and as part of a regular quality assurance (QA) program (Pike *et al* 2013, Armstrong and Eadie 2015). For clinical trials additional quality control (QC) tests are often performed to ensure compliance and equivalence between systems at different centres (Kaalep *et al* 2018).

Single Photon Emission Computed Tomography (SPECT) and Positron Emission Tomography (PET) imaging systems have developed significantly over the last decade, particularly with improvements in quantitative imaging. However, there has been little development in the quality control procedures used to validate these systems. A major hindrance in quality control is the complexity and time required to prepare phantoms for the specific tests. Phantoms used for QC often require complex preparation of radioactive

sources placed within a variety of geometries. As a result, quality assurance can be considerably time consuming and minor mistakes and inconsistencies in source preparation or timing can result in tests becoming invalid. This can potentially result in an extended period of system down time or may cause a delay in the commencement of clinical trials. Phantoms containing sealed sources with relatively long half-lives such as Co-57 and Ga-68 enable tests to be performed without complex source preparation. However, only simple source geometries are available and therefore the number of performance tests which can utilise these phantoms are limited.

Additive manufacturing technology has been proposed as a means to overcome some of these limitations by allowing the production of more complex geometries with a lower cost constraint compared to conventional production (Ehler *et al* 2018). Liquid fillable phantoms with complex geometries, including anatomically realistic test objects generated from patient Computed Tomography (CT) data, have previously been constructed using rapid prototyping technology (Gear *et al* 2014, 2016, Tran-Gia *et al* 2016, Filippou and Tsoumpas 2018, Price *et al* 2019, Kuhnel *et al* 2020). However, these designs still require dilution and preparation of the radionuclide into different phantom compartments before construction. Additive manufacturing phantoms by DiFilippo (DiFilippo *et al* 2004) *et al* and Cox *et al* (Cox *et al* 2016), demonstrated unique designs to overcome this constraint. These used sub-resolution inserts and filling designs that allowed a heterogeneous activity distribution be filled from a single port and activity dilution.

Complex heterogeneous activity distributions generated within 2-dimensional test objects were proposed by Larsson *et al* (Larsson *et al* 2000) and van Staden *et al* (van Staden *et al* 2007) by incorporating radiopharmaceuticals into the ink of a commercial ink-jet printer. It was demonstrated that complex geometries and concentrations could be simulated in a printed phantom with minimal operator interaction. 3D versions were also proposed (Markiewicz *et al* 2011, Bieniosek *et al* 2015) by stacking the 2D printed sheets between spacer material, or placing them in orthogonal planes. However, this process still required a significant degree of manual operation to construct the 3D object from the 2D printed sheets.

Integration of radiopharmaceuticals directly into the print material of a 3D printer combines the advantage of the 2D printed ink methodology with the versatility of 3D design available with additive manufacturing. Polyjet technology is a form of additive manufacturing (3D printing) that uses a combination of stereo-lithography and inkjet technology. A 28 micron layer of liquid ultraviolet curable photopolymer is printed onto a build tray. An ultraviolet light cures the resin solidifying the pattern traced on the tray. This process is repeated printing each layer of photopolymer onto the last and curing with the light until a 3D object is formed. It was previously demonstrated that polyjet technology can be used for printing water tight phantoms (Gear *et al* 2014) and is therefore a suitable material to trap a radioactive compound into a 3D printed design. The aim of this work was to demonstrate the feasibility of manufacturing molecular imaging test objects by directly incorporating radioisotopes within the liquid photopolymer. This procedure will allow the generation of PET and SPECT performance test objects with complex 3D activity distributions (Larsson *et al* 2000, El-Ali *et al* 2003, Negus *et al* 2016).

## 2. Method

### 2.1. Initial tests

The printing material used within a Polyjet printer is a photo-curable polymer. This is an acrylate resin of uncured thermoset polymer that undergoes chemical transformation into a cross-linked polymer through a free radical chain reaction when exposed to light.

Free radical polymerisation can also be induced in materials by exposure to ionising radiation (Gear *et al* 2006). Polymerisation can also be adversely inhibited with the presence of contaminants such as molecular oxygen through the quenching of free radicals (Gear *et al* 2006). It therefore follows that the introduction of radiopharmaceuticals into the resin could cause an unstable response, either inhibiting polymerisation or initiating premature curing and potentially destroying the printed object or the printer itself.

To test the stability of the resins and explore the optimal method of introducing the radiopharmaceutical the response to external factors including ionising radiation, light and dilution was explored. Two batches of 100 ml of photo-polymer were extracted from the print cartridges of an Objet30 Pro 3D printer. Resins used in the tests and for subsequent printing were 'build' resin (Exo-1,7,7-trimethylbicyclo[2.2.1]heptyl acrylate, Octahydro-4,7-methano-1 H-indenediyl)bis(methylene)diacrylate) (trade name VeroWhitePlus™, RGD835) and 'support' resin (Tris (N-hydroxy-N-nitrosophenylamino-O,O') aluminium) (Trade name Support™, SUP705) (Stratasys, Rehovot, Israel).

**Table 1.** Summary of types of exposure to each of 10 vials in the two batches of resin investigated (Build and Support resin).

Vial Number (for each batch of resin)	Exposure
1–6	6 MV photon beam (5–50 Gy)
7	120 MBq Tc-99m
8	Natural daylight
9–10	Control

Ten grams of each material were sub-dispensed into 10 P6 nitrogen vials. Exposure to air and light was limited during extraction to reduce undesirable polymerisation. When not in use all vials were stored within a dark lead lined safe for the duration of the study.

Six of the vials from each batch were externally irradiated approximately 24 h post extraction using an Elekta Versa HD linear accelerator (Elekta AB, Stockholm, Sweden), under reference conditions. A 6 MV photon beam with a  $10 \times 10 \text{ cm}^2$  field was used to irradiate the vials from 5 to 50 Gy.

120 MBq of [ $^{99\text{m}}\text{Tc}$ ]pertechnetate in 0.1 ml were added to a vial of each resin and gently agitated before imaging on a Siemens Symbia Intevo gamma camera (Siemens Healthcare GmbH, Erlangen, Germany). Images were acquired for 1 min for the first 300 min then for 10 min per frame up to 20 h post preparation. Acquisitions were acquired with a  $256 \times 256$  matrix, and 3.2x image zoom giving a pixel size of 0.75 mm.

Regions of interest (ROIs) were placed at the top and bottom of the vials on the images and the ratio of counts in each region used to measure any change in activity distribution over the duration of the imaging. This was used to determine any potential separation or settling of the Tc99m within the polymer.

Two vials of each material were kept as controls in the safe and not exposed to any external factors. A single vial of each material was stored in a radiation free environment and exposed to natural daylight. Visual and viscosity changes of polymer consistency within all vials were recorded for a period of 3 weeks post extraction from the cartridge. Following the observation period all vials were placed under a ultraviolet (UV) lamp and any potential inhibition in polymerization recorded. A summary of the exposure to the 10 vials from each batch of resin is summarised in table 1.

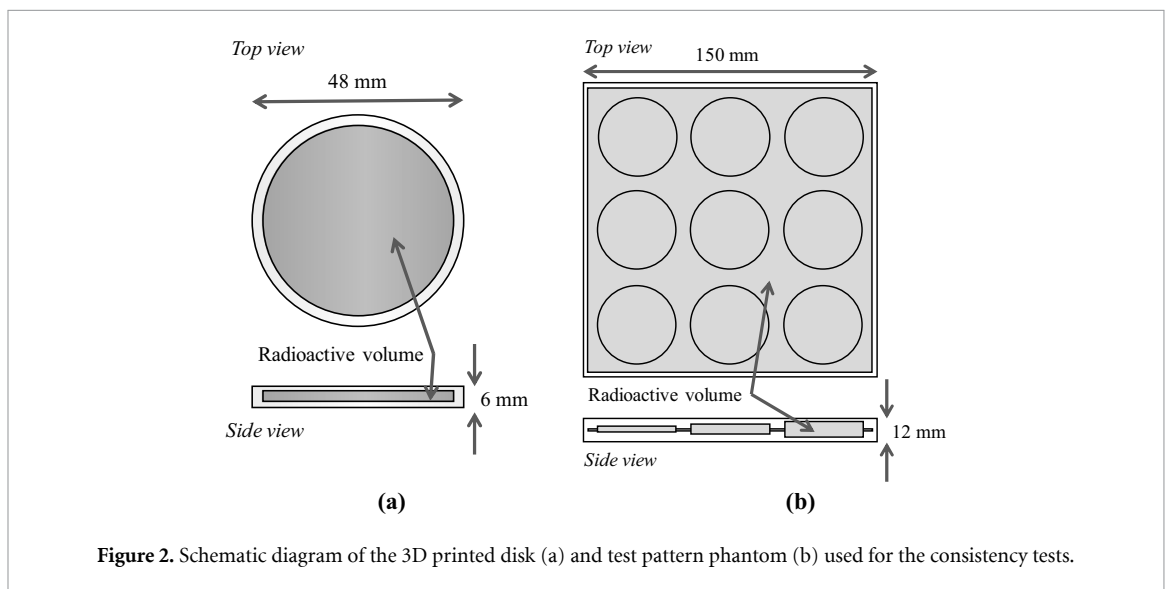
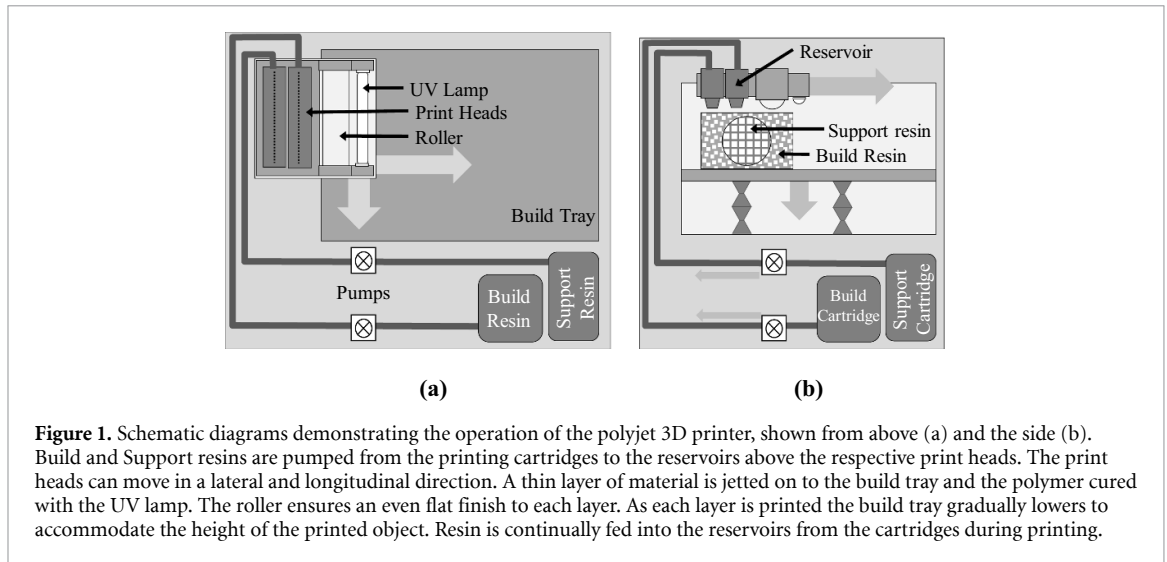
## 2.2. Printing

Following the successful integration and stability tests, the support resin was selected as the desired radioactive material. This allowed phantoms to be designed containing a radioactive central section, surrounded by a non-radioactive outer covering. During printing, the printer automatically fills hollow sections with support material, thereby allowing the creation of a radioactivity distribution of the desired design. A schematic diagram demonstrating the operation of the printer is given in figure 1. Various phantoms were conceived to explore the operational performance of the printer and to test the printed parts for suitability as imaging test objects. For each test, a geometrical solid object (rectangular or cylindrical) containing a more complex void or hollow central section was designed using Autodesk Inventor (2019). A detailed description of each phantom is given in the following sections. For each phantom test a separate print run was required. For each print run 1000 MBq of [ $^{99\text{m}}\text{Tc}$ ]pertechnetate were injected into the printer support resin cartridge of an Objet 30pro polyjet printer (Stratasys, Rehovot, Israel). Following injection the cartridge was gently agitated for 2 min using a Grant Bio PMR-30 Platform Rocker (Grant Instruments, Cambridgeshire, UK). The printing cartridge was then reinserted into the 3D printer and the material change procedure performed. The change procedure pumps the new material through the printer filling tubes and into the material reservoirs located above the printing heads. During this procedure non-radioactive resin previously contained within the printer is purged from the system and replaced with the radioactive solution.

## 2.3. Concentration consistency

To test the quality of the system purge and to ensure a consistent concentration of Tc-99m could be achieved, 12 disks, 48 mm in diameter and 6 mm in height, were consecutively printed. Within each disk a central section containing 6.6 ml of radioactive support resin was printed. A schematic diagram of a disk is shown in figure 2(a)

After all disks were printed each disk was individually measured in a Capintec CRC-15 dose calibrator (Mirion Technologies, NJ, US). 10 ml of unused resin was then extracted from the printer cartridge and the activity also measured. The concentration within the printed disks and unprinted resin were then compared. Mass measurements of each disk were performed to ensure printing consistency between pieces. Scintigraphic images of the disks were captured on a Siemens Intevo gamma camera equipped with low energy high resolution collimators. The circular faces of the printed disks were placed on the surface of the



collimator and acquisitions acquired for 300 s with a  $256 \times 256$  matrix. Regions of interest were placed within the central region of each disk and the total counts within each ROI recorded.

#### 2.4. Test pattern consistency

To measure the consistency and precision of the printing procedure, and to demonstrate the potential of producing heterogeneous test patterns, a design analogous to the Williams liver phantom was conceived. A 12 mm thick,  $150 \times 150$  mm, square phantom was printed containing a  $148 \times 148$  mm active square region 1 mm thick. Within the active region an array of 40 mm diameter cylinders were placed with increasing thicknesses of 2 to 10 mm representing regions of increasing contrast from 2:1 to 10:1. A schematic diagram of the phantom is shown in figure 2(b)

Post production scintigraphic images of the phantom were acquired with the square face of the phantom placed on the surface of a low energy high resolution collimator and a 6.8 million count acquisition performed with a  $512 \times 512$  matrix and image zoom of 2x giving an pixel size of 0.6 mm. Four regions of interest were placed within the background area of the phantom and 9 additional ROIs within areas corresponding to the positions of the cylinders. Total counts within each ROI were recorded and compared to the designated thickness of active print material in that region.

#### 2.5. Uniformity

To test the uniformity of the printing process a 2 mm thick rectangular phantom ( $192 \text{ mm} \times 292 \text{ mm}$ ) covering the largest possible printable area of the printer was produced. The phantom contained a central active region 1 mm thick and  $190 \text{ mm} \times 290 \text{ mm}$  in area. Post production scintigraphic images of the phantom were acquired with the phantom placed on the collimator surface and a 30 million count

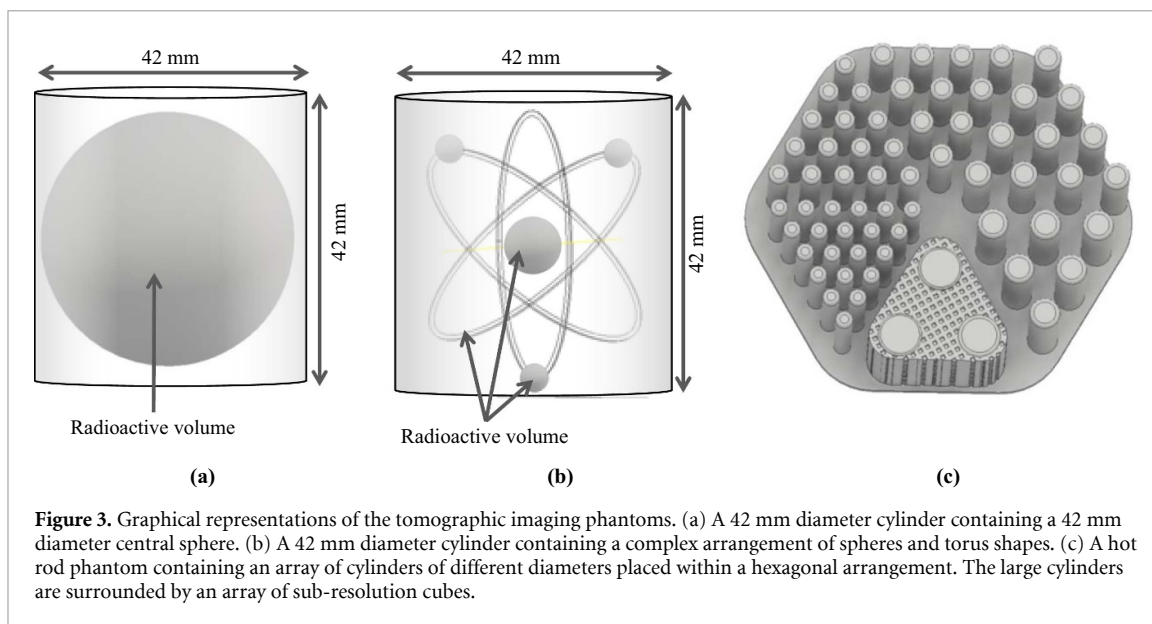


**Figure 3.** Graphical representations of the tomographic imaging phantoms. (a) A 42 mm diameter cylinder containing a 42 mm diameter central sphere. (b) A 42 mm diameter cylinder containing a complex arrangement of spheres and torus shapes. (c) A hot rod phantom containing an array of cylinders of different diameters placed within a hexagonal arrangement. The large cylinders are surrounded by an array of sub-resolution cubes.

acquisition performed with a  $512 \times 512$  matrix size and image zoom of 2 giving a pixel size of 0.6 mm. For comparison a similar acquisition was performed with a Co-57 large field-of-view flood phantom (RadLite, RadQual™, Idaho, US). Uniformity was assessed by measuring the integral uniformity in the central region of the phantom ( $180 \times 280$  mm) according to the specification described by The Association of Electrical Equipment and Medical Imaging Manufacturers (NEMA NU 1–2018). Line profiles were also taken along the horizontal and vertical axes of the images to visualise any patterns of non-homogeneity.

## 2.6. Heterogeneous SPECT phantoms

The predominant advantage in this technology is the ability to produce 3 dimensional activity distributions for performance evaluation of tomographic imaging systems. To demonstrate this potential two cylindrical phantoms were printed within which a centralised region of radioactivity was contained. The first phantom contained a simple sphere, 40 mm in diameter and the second, contained a 10 mm central sphere, with three 5 mm diameter spheres placed in orthogonal planes about the central region. The smaller spheres were connected via a 1 mm thick torus orbiting the central sphere. The central sphere contained a lower activity concentration than the outer spheres by constructing it from an array of sub-resolution interlacing cubes, 0.1 mm in size. A graphical representation of these activity distributions are given in figures 3(a) and (b).

A third larger phantom was printed based on the Jaszczak and Derenzo phantoms. A hexagonal arrangement of cylinders 5 cm in height were printed with cylinder diameters of 5.1, 6.3, 7.6, 8.9, 10.2 and 15.3 mm, each with a 1 mm wall of non-active material. Within the sextant surrounding the largest cylinders a volume was designed to simulate lower source to background contrast. This was achieved by printing an array of sub-resolution interlacing cubes, 1 mm in size about the rods. A graphical representation of this phantom is given in figure 3(c). The longest axis of the phantom was 150 mm.

Tomographic images were acquired with the phantoms suspended beyond the end of the imaging couch. Detectors contoured about the perimeter of the phantom in 64 projections, with a  $256 \times 256$  imaging matrix and detector zoom of 2x, giving a pixel size of 1.2 mm. Images were reconstructed using the Siemens FLASH 3D OSEM iterative algorithm for 20 iterations and 8 subsets using a Gaussian modelled collimator detector response, CT attenuation correction and dual energy window scatter correction. To obtain an image with higher contrast and improved resolution, a planar scintigraphic acquisition was also performed of the hot rod phantom with the phantom placed on the collimator surface, orientated with the rods perpendicular to the detector plane.

## 3. Results

### 3.1. Initial tests

Photographs of the vials containing support and build resins, prior to curing, are shown in figure 4. Observed long term stability of print material outside the print cartridge was promising with no notable changes in the support or build resins after 3 weeks. No viscosity or visual changes in material were observed for any of the vials exposed to irradiation up to 50 Gy, provided exposure to natural daylight was avoided.

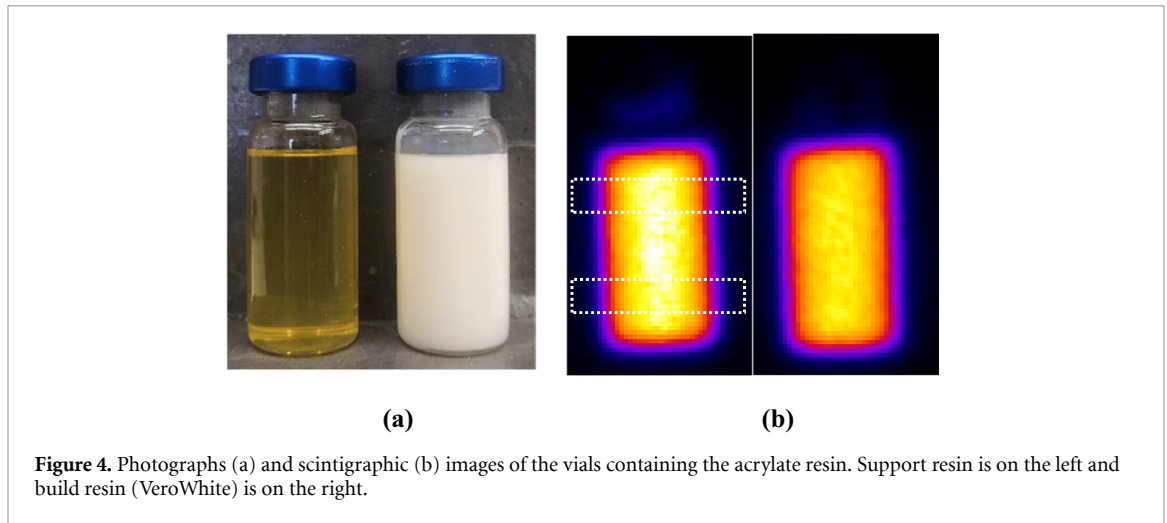


**Figure 4.** Photographs (a) and scintigraphic (b) images of the vials containing the acrylate resin. Support resin is on the left and build resin (VeroWhite) is on the right.

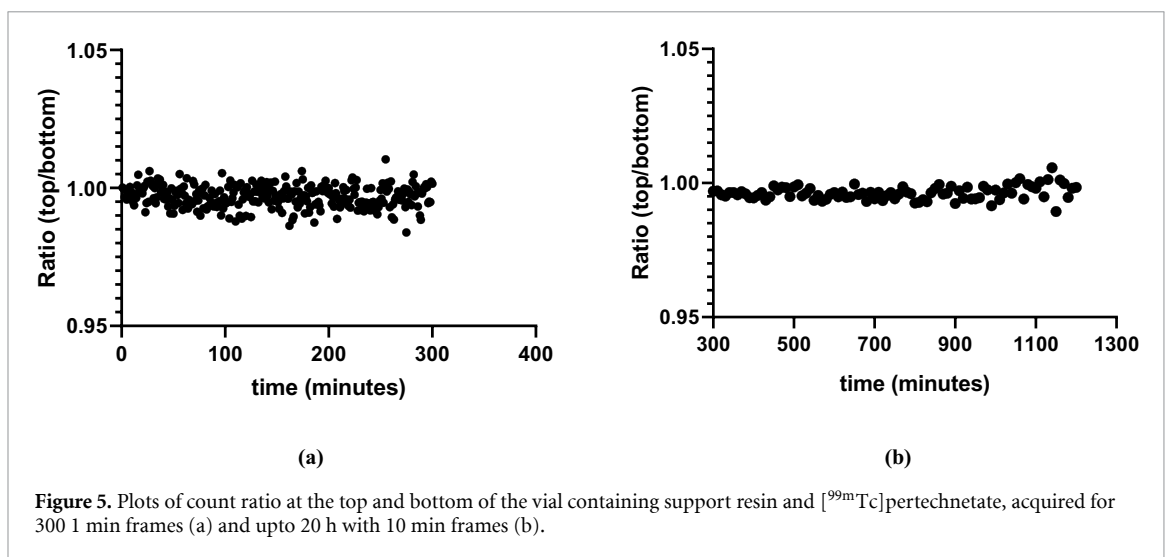


**Figure 5.** Plots of count ratio at the top and bottom of the vial containing support resin and  $[^{99m}\text{Tc}]$ pertechnetate, acquired for 300 1 min frames (a) and upto 20 h with 10 min frames (b).

When exposed to natural light a thin film began to form at the periphery and surface of the polymer which completely solidified after 2 h.

Integration of  $[^{99m}\text{Tc}]$ pertechnetate into the material was successful and a uniform concentration was achieved by gently agitating the mixtures for a few seconds. The uniform distribution of Tc99m in the resin is demonstrated in figure 4(b), for a vial of support (left) and build (right) resin. After 24 h no significant separation of Tc99m was observed in either vial. Figure 5 shows plots of the ratio of counts over time within regions at the top and bottom of the vial containing the support resin. The position of the ROIs are shown in figure 4(b). All vials polymerised as expected within a few seconds when exposed to UV light indicating that the presence of  $[^{99m}\text{Tc}]$ pertechnetate and exposure to ionising radiation did not affect the properties of the photopolymer.

### 3.2. Concentration consistency

Integration of the radio-polymer into the printer was successful. Figure 6 shows the scintigraphic images of the first six 3D printed disks. Each disk took 40 min to print following the initial system purge. A reasonable uniformity in each disk is observed. The masses of the disks were consistent, at  $12.52 \text{ g} \pm 0.01 \text{ g}$  (Average  $\pm$  SD), with a coefficient of variation of 0.08%. Measured activity within the disks increased with increasing print number. This was also the case for the measured counts within the central region of each disk. Count and disk activity followed a sigmoidal function, (figure 7) indicating that the concentration of the Tc-99m within the resin was increasing with material use. This can be attributed to a remainder of non-radioactive resin present within the printer reservoir that still mixed with the radio-polymer after the purge sequence. A consistent concentration was observed after disk 5, at which point approximately 60 g of support material had been used. After the initial prints, the measured activity of the disks agreed within  $98 \pm 2\%$  of the expected activity. The coefficient of variation between printed disks was less than 1%.

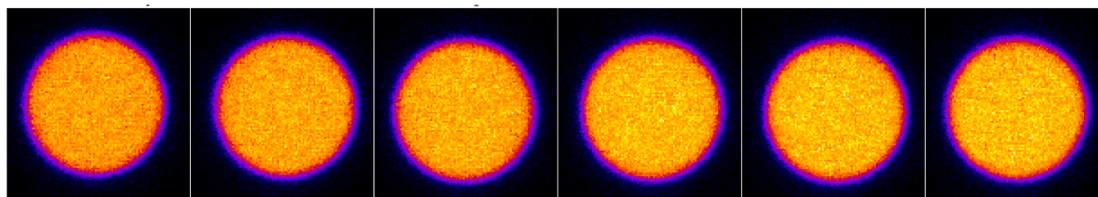


Figure 6. Scintigraphy images of first six 3D printed disks. Each disk was printed consecutively from left to right.

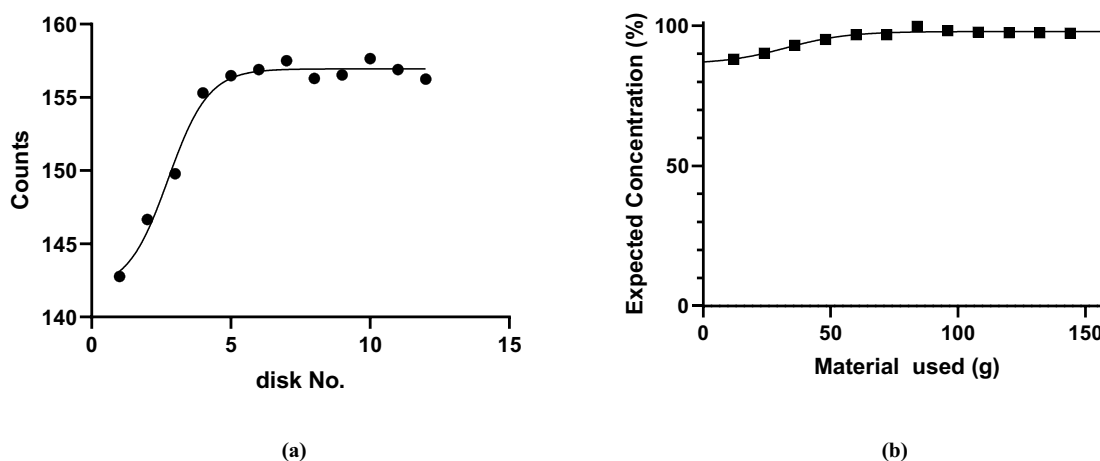


Figure 7. Plots of counts (a) and activity (b) measured from the printed disks.

### 3.3. Test pattern consistency

The acquired image of the test pattern phantom is given in figure 8(a) where the radioactive central square and array of more active circular regions are clearly evident. The measured counts within these regions plotted against source depth, exhibits a linear relationship as shown in figure 8(b). This result demonstrates the ability of the printing method to predictably replicate radioactive source distributions at varying contrasts and activity levels.

### 3.4. Uniformity

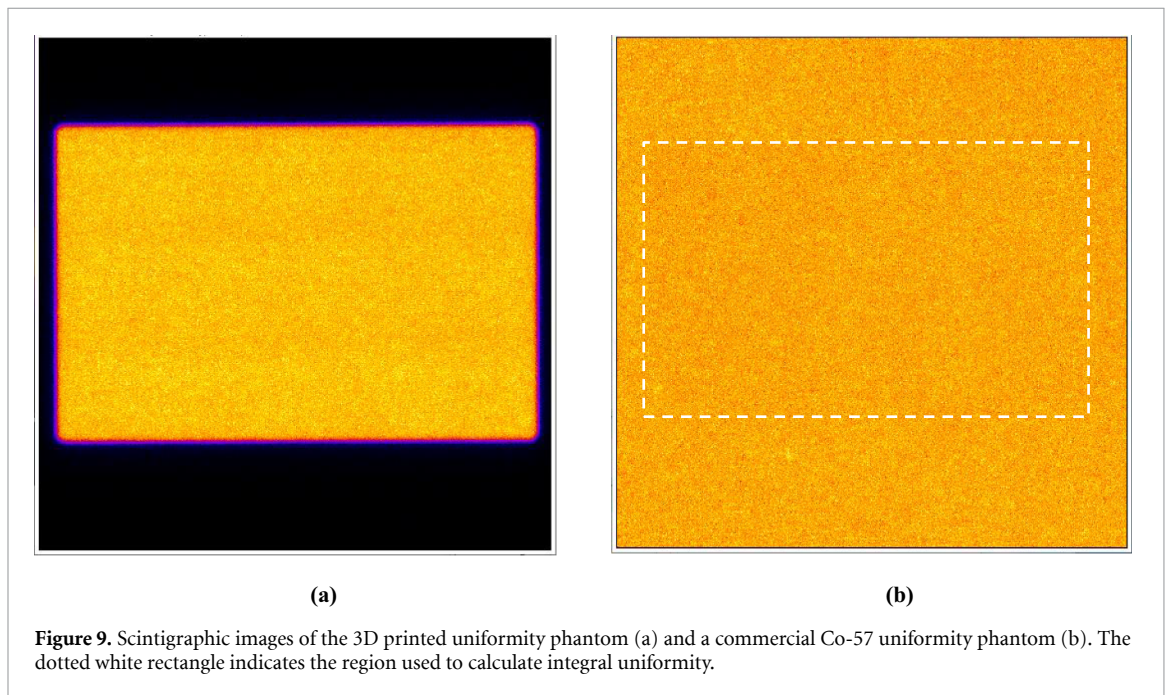
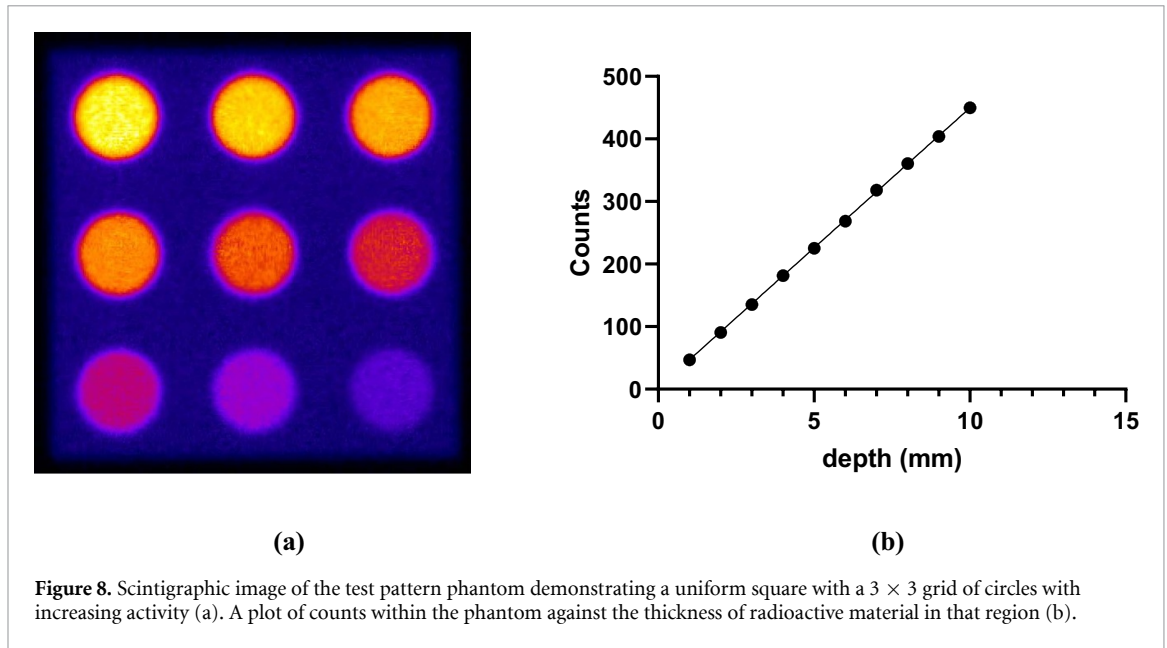
Figure 9 shows the scintigraphic image of the 3D printed uniformity phantom, alongside the corresponding Co-57 flood phantom. Profiles across these images are given in figure 10. For easier visual comparison counts used to generate the profiles from the Co-57 image have been rescaled to be just above that generated from the printed phantom.

The printed phantom was insufficient to cover the whole detector field of view, due to the limitation of print size. The total print time for this piece was 2 h. Integral uniformity within the central sections of the phantom were 5.2% and 6.0% for the 3D printed and commercial phantoms respectively. Whilst the values of integral uniformity are comparable for both phantoms a degree of heterogeneity is observed in the 3D printed phantom evident in the horizontal and vertical profiles shown in figure 10. Most prominent are the horizontal bands of reduced activity across the length the phantom. The position of these bands coincides with the width of the printer head and is attributed to a slight deviation in material dispersion and overlap of passes in printer head motion.

A slight decrease in counts is observed across the horizontal length of the printed phantom (figure 10(a)). However comparison with a similar profile across the Co-57 phantom demonstrates an equivalent pattern, indicative of a sensitivity variation in the detector rather than a non-uniformity in the phantom.

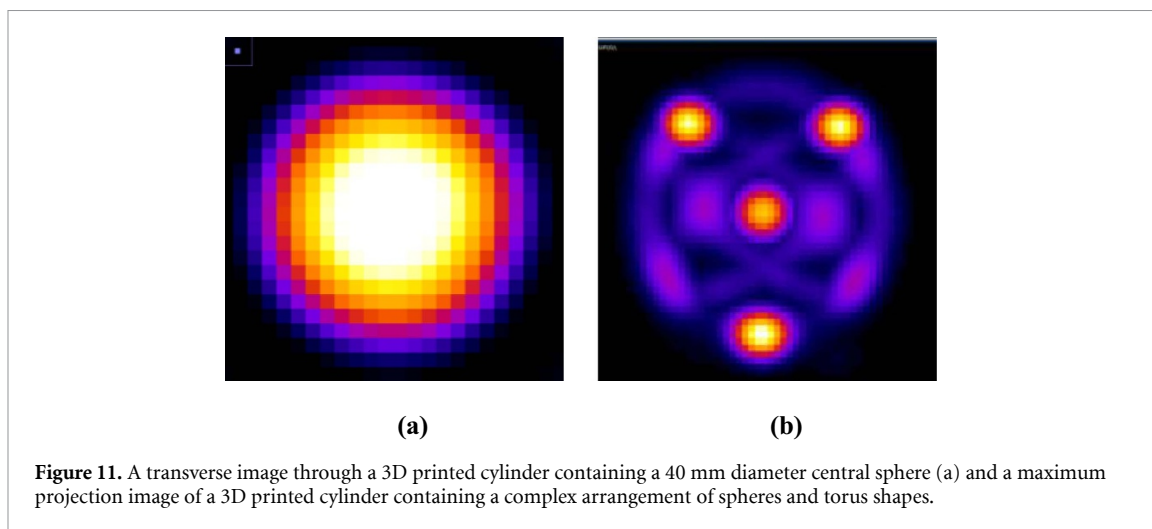
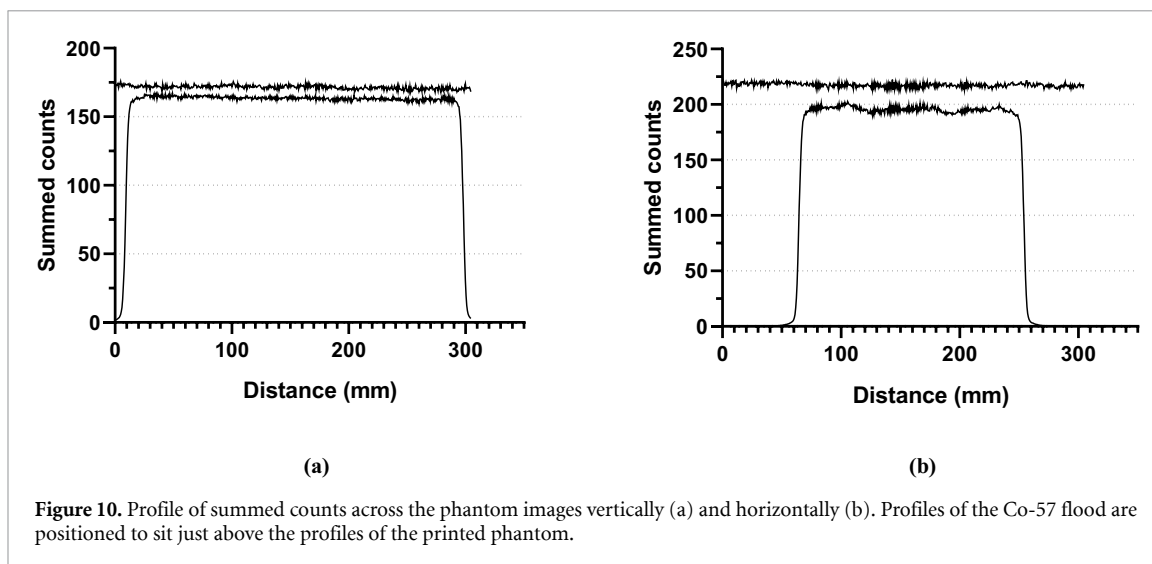
### 3.5. SPECT imaging

Reconstructed images of the tomographic data acquired about the 3D printed SPECT phantoms are shown in figure 11 for a transverse slice through the uniform sphere (figures 11(a)) and (b) maximum intensity projection of the heterogeneous distribution (figure 11(b)). These images clearly demonstrate the ability to produce both uniform and complex activity distributions in 3-dimensions, to a scale and resolution unattainable from traditional methods of phantom production. In figure 11(b) the sub-resolution nature of



the phantom is apparent. The 10 mm central sphere is indistinguishable in size and contrast from the 5 mm diameter outer spheres due to the poor resolution of the SPECT image.

A photograph of the hot rod phantom is given in figure 12(a) with CT and SPECT images in figures 12(b) and (c). The planar scintigraphic acquisition is also given in figure 12(d). All rods are clearly visible on the CT acquisition with a uniform activity concentration observed in the rods on the SPECT and planar datasets. Individual rods are visible in 5 of the sextants on the SPE scan with a spatially variant detector response resulting in higher counts in rods situated at the periphery of the phantom. The sextant with background activity surrounding the larger rods is clearly visible on the planar scintigraphy image and has a uniform appearance. Attenuation properties of the support and build materials are similar (density =  $1.17 \text{ g cm}^{-3}$ ), the brighter edge at the periphery of the rods in figure 12(b) is a sharpening artefact rather than a difference in attenuation between the two resins. In the sextant containing the largest rods, with background activity, the slight attenuation difference between the support and build resins is evident. For an ROI placed centrally within a rod the measured Hounsfield unit was 83 HU compared to 102 HU within the central volume of the sextant. The cubic arrays used to produce a lower activity concentration are marginally



visible on the CT image but indistinguishable on any of the scintigraphic acquisitions, demonstrating the validity of using this technique to produce areas of differing activity concentrations.

#### 4. Discussion

This work has shown that radiopharmaceuticals can be incorporated into a photo-curable polymer and used within a polyjet 3D printer to produce a variety of radioactive phantoms. To our knowledge this is the first time that molecular imaging phantoms have been directly printed using this technology and their application demonstrated. Lappchen *et al* recently published a method for integrating [ $^{99m}\text{Tc}$ ]pertechnetate solution into a similar photopolymer that required a separation of phases and chemical removal of traces of water (Lappchen *et al* 2020). This work has demonstrated that a uniform and stable consistency could be achieved by simply gently mixing the two solutions. The material was also shown to be stable outside of the printer and that exposure to ionising radiation did not unduly affect the properties of the resin. The only uncontrolled polymerisation occurred when the resin was exposed to natural daylight. This limitation was easily avoided by mixing the Tc99m directly into the print cartridge. Use of the radio-polymer within a Polyjet printer was achieved without the need of directly radiolabelling the isotope to the polymer. As the solution is jetted onto the build tray the trace amounts of isotope mixed within the resin are uniformly distributed and then trapped within the polymer matrix when cured. Uniformity of the print was demonstrated by producing a 1 mm flat rectangular phantom which showed favourable uniformity compared to a commercial Co-57 flood phantom. Although some slight non-uniformity was observed (attributed to overlap of printer head during print passes) this would likely be resolved when printing deeper phantoms where more passes of the printer head would occur. No undesirable non-uniformities were observed in any of the other test phantoms produced in this study.

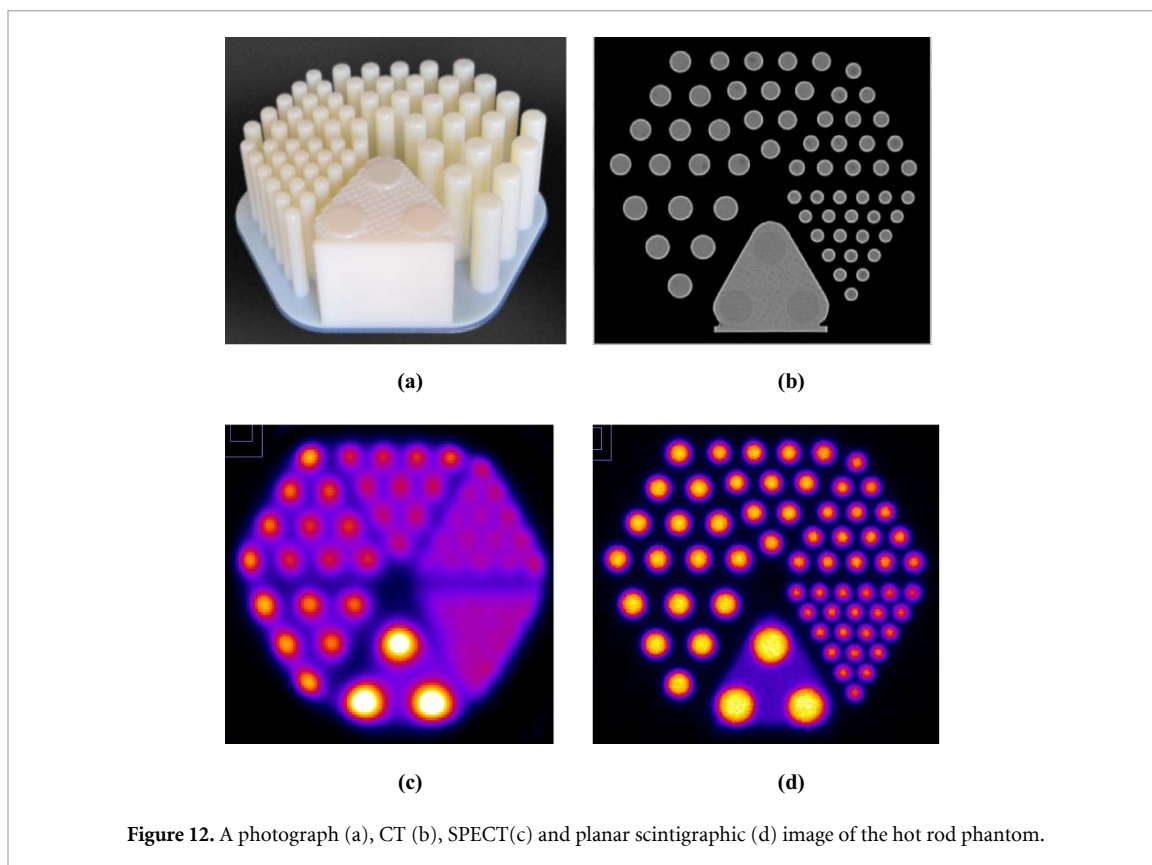


Figure 12. A photograph (a), CT (b), SPECT(c) and planar scintigraphic (d) image of the hot rod phantom.

A variety of 3D printed test objects were produced. Similar approaches have been proposed by Miller *et al* (Miller and Hutchins 2009) who demonstrated the ability to add F18 FDG into the binder used in a powder deposition 3D printer and Lappchen *et al* (Lappchen *et al* 2020) who produced simple geometrical shaped phantoms using a ProJet® 1200 3D Printer. In both these studies the phantoms produced were limited to uniform activity distributions. In this work phantoms were produced with complex heterogeneous activity distributions, including those suitable for evaluating, system uniformity, contrast, resolution, recovery and sensitivity. Example activity distributions were generated in a test pattern phantom imaged in 2D with regions of different activity contrasts (figure 8) and the hot rod phantom of figure 12. A complex activity distribution consisting of concentric torus shapes and spheres orbiting a central region of activity (figure 11(b)) was also produced. As the radioactivity was incorporated into the support resin of the 3D printer it was possible to form these complex geometries, including sub-resolution geometries to simulate areas of different activity concentrations (figure 12). These designs could not have been reproduced using conventional phantom production.

There are challenges associated with this approach that stem largely from the fact that the support resin is designed to be a waste material, which is easily removable from the printed object. When producing 3D pieces support material is used to fill voids or overhangs to stop the object collapsing during printing. In this project this design feature was exploited to create the desired activity distribution. However, this also means that for any objects printed for which an overhang exists additional radioactive support will be printed on the outside of the object. Indeed for each piece produced a ‘carpet’ of support is first placed on the build tray which allows the final piece to be easily removed. Whilst radioactive, care must be taken to remove any support material or debris left on the build tray after manufacture. In addition the 3D printed object had to be thoroughly cleaned and decontaminated prior to use. After cleaning and removal of unwanted support material no residual surface contamination was found on the printed pieces (wipe tested with an alcohol swab placed 1 cm from the entrance window of an EP15 scintillation detector (Mini Instruments UK)). Operator time spent preparing the printer and cleaning the final printed pieces was still considerably lower than that required to prepare traditional phantoms for imaging.

In this work the printer used was only capable of printing two materials (build and support). To generate different activity concentrations a sub-resolution voxel approach was implemented, similar to that proposed by DiFilippo *et al* (DiFilippo *et al* 2004). DiFilippo *et al* produced a PET phantom with sub resolution cold rods. When filled with radioactive solution the volumes containing the rods demonstrated lower activity. The difficulty faced with that design is that air gaps can arise between rods due to surface tension between the

water. With 3D printing a sub-resolution cubic arrangement can be designed to achieve the same effect, but without the difficulty of having to fill the small voids.

Multi-material printers have become available which can mix build materials of different optical and tensile properties during printing. This ability would overcome the challenges previously mentioned as the radioisotope could be mixed into a single colour build resin (for example black). The removable support material would remain non-radioactive and a phantom could be designed with different shades of 'grey' equivalent to different activity concentrations.

A further complication is the potential waste produced during manufacture. To ensure a consistent concentration of Tc-99m in the resin the non-radioactive print material must first be removed from the printer. The material change procedure purges unwanted resin by pumping the radioactive solution from the cartridge into the printing heads. This procedure results in the waste of approximately 200 g of material for each change of material, which is potentially a wasteful and costly procedure if a short lived isotope is used for a small object. This purge procedure is not entirely successful and at first use a slight variation in activity was observed in repeated prints of identical objects. As the printed objects were directly measured in a radionuclide dose calibrator, activity concentration was therefore traceable to national primary standards. Mass measurements of these pieces showed no difference in total material used which validates the conclusion that the activity concentration was changing. This limitation was overcome by flushing more material through the printer before manufacture. After the initial few prints these activities were shown to agree favourably with the expected activity concentration. Provided care is taken to ensure consistency across prints, phantoms can be produced with a desired activity concentration and contrast.

Whilst there are some technical challenges associated with producing phantoms in this way, the potential benefits are clearly evident. Where the technology will likely become more mainstream is for the production of phantoms containing long-lived isotopes such as Ge-68 or Co-57. This will negate some of the time constraints associated with 3D printing and will allow the production and distribution of phantoms from a central source or provider. The increased resolution and ability to produce quantified heterogeneous distributions will allow more advanced phantoms to be produced for both clinical and pre-clinical use. In addition to anthropomorphic and anatomically based phantoms, generic designs could be conceived that are capable of simultaneously testing system uniformity, resolution, and contrast for PET and SPECT scanners.

3D printing has seen a dramatic increase in use in the medical sector and the interest of its application for producing phantoms will continue to increase. It is not unreasonable to envisage additive manufacturing eventually replacing the conventional methods of phantom manufacture (Ehler *et al* 2018).

## 5. Conclusions

Tc-99m has been successfully integrated into the photopolymer of a 3D printer and radioactive phantoms created. It was demonstrated that a uniform, reproducible activity distribution can be created in addition to complex heterogeneous activity distribution. Phantoms were created suitable for evaluating system uniformity, contrast, resolution, recovery and sensitivity. This technology could revolutionise phantom production and lead to more rigorous QC of molecular imaging systems.

## Acknowledgments

This work was supported by the Institute of Physics and Engineering in Medicine (Innovation Grant 2019). We acknowledge support from the NIHR RM/ICR Biomedical Research Centre.

## ORCID iD

Glenn D Flux  <https://orcid.org/0000-0003-4743-2276>

## References

- Armstrong I S and Eadie E 2015 *Quality Control of Gamma Cameras and Nuclear Medicine Computer Systems: A Report Produced by the Institute of Physics and Engineering in Medicine* (York: Institution of Physics & Engineering in Medicine & Biology)
- Bieniosek M F, Lee B J and Levin C S 2015 Technical note: characterization of custom 3D printed multi-activity imaging phantoms *Med. Phys.* **42** 5913–8
- Cox B L *et al* 2016 Development of a novel linearly-filled Derenzo microPET phantom *Am. J. Nucl. Med. Mol. Imaging* **6** 199–204
- DiFilippo F P, Price J P, Kelsch D N and Muzic R F 2004 Porous phantoms for PET and SPECT performance evaluation and quality assurance *Med. Phys.* **31** 1183–94
- Ehler E, Craft D and Rong Y 2018 3D printing technology will eventually eliminate the need of purchasing commercial phantoms for clinical medical physics QA procedures *J. Appl. Clin. Med. Phys.* **19** 8–12

- El-Ali H, Ljungberg M, Strand S-E, Palmer J, Malmgren L and Nilsson J 2003 Calibration of a radioactive ink-based stack phantom and its applications in nuclear medicine *Cancer Biother. Radiopharm.* **18** 201–7
- Filippou V and Tsoumpas C 2018 Recent advances on the development of phantoms using 3D printing for imaging with CT, MRI, PET, SPECT, and ultrasound *Med. Phys.* **45** E740–60
- Gear J I et al 2016 Abdo-man: a 3D-printed anthropomorphic phantom for validating quantitative SIRT *EJNMMI Phys.* **3** 17
- Gear J I, Flux G D, Charles-Edwards E, Partridge M, Cook G and Ott R J 2006 The application of polymer gel dosimeters to dosimetry for targeted radionuclide therapy *Phys. Med. Biol.* **51** 3503–16
- Gear J I, Long C, Rushforth D, Chittenden S J, Cummings C and Flux G D 2014 Development of patient-specific molecular imaging phantoms using a 3D printer *Med. Phys.* **41** 525–7
- Kaalep A, Sera T, Oyen W, Krause B J, Chiti A, Liu Y and Boellaard R 2018 EANM/EARL FDG-PET/CT accreditation - summary results from the first 200 accredited imaging systems *Eur. J. Nucl. Med. Mol. Imaging* **45** 412–22
- Kuhnel C, Seifert P, Mulik C, Winkens T and Freesmeyer M 2020 3D printing of fillable individual thyroid replicas based on nuclear medicine DICOM data used as phantoms for gamma probe calibration *Nuklearmedizin Nucl. Med.* **59** 12–19
- Lappchen T, Meier L P, Fürstner M, Prenosil G A, Krause T, Rominger A, Klaeser B and Hentschel M 2020 3D printing of radioactive phantoms for nuclear medicine imaging *EJNMMI Phys.* **7** 22
- Larsson S A, Jonsson C, Pagani M, Johansson L and Jacobsson H 2000 A novel phantom design for emission tomography enabling scatter- and attenuation-“free” single-photon emission tomography imaging *Eur. J. Nucl. Med.* **27** 131–9
- Markiewicz P J, Angelis G I, Kotasidis F, Green M, Lionheart W R, Reader A J and Matthews J C 2011 A custom-built PET phantom design for quantitative imaging of printed distributions *Phys. Med. Biol.* **56** N247–61
- Miller M A and Hutchins G D 2007 Development of anatomically realistic PET and PET/CT phantoms with rapid prototyping technology 2007 *IEEE Nuclear Science Symp. Conf. Record (Honolulu, HI, 2007)* (Piscataway, NJ: IEEE) pp 4252–7
- Negus I S, Holmes R B, Jordan K C, Nash D A, Thorne G C and Saunders M 2016 Technical note: development of a 3D printed subresolution sandwich phantom for validation of brain SPECT analysis *Med. Phys.* **43** 5020–7
- Pike L et al 2013 *Quality Assurance of PET and PET/CT Systems* (York: Institution of Physics & Engineering in Medicine & Biology)
- Price E, Robinson A P, Cullen D M, Tipping J, Calvert N, Hamilton D, Oldfield C, Page E, Pietras B and Smith A 2019 Improving molecular radiotherapy dosimetry using anthropomorphic calibration *Physica Med.* **58** 40–46
- Tran-Gia J, Schlogl S and Lassmann M 2016 Design and fabrication of kidney phantoms for internal radiation dosimetry using 3D printing technology *J. Nucl. Med.* **57** 1998–2005
- van Staden J A, Raan H D, Lötter M G, Aswegen A V and Herbst C P 2007 Production of radioactive quality assurance phantoms using a standard inkjet printer *Phys. Med. Biol.* **52** N329–37